



HAL
open science

Estimating perturbed stress from 3-D borehole displacements induced by fluid injection in fractured or faulted shales

Yves Guglielmi, Christophe Nussbaum, Jonny Rutqvist, Frédéric Cappa, Pierre Jeanne, Jens Birkholzer

► **To cite this version:**

Yves Guglielmi, Christophe Nussbaum, Jonny Rutqvist, Frédéric Cappa, Pierre Jeanne, et al.. Estimating perturbed stress from 3-D borehole displacements induced by fluid injection in fractured or faulted shales. *Geophysical Journal International*, 2020, 221 (3), pp.1684-1695. 10.1093/gji/ggaa103 . hal-02520903

HAL Id: hal-02520903

<https://hal.science/hal-02520903v1>

Submitted on 27 Mar 2020

HAL is a multi-disciplinary open access archive for the deposit and dissemination of scientific research documents, whether they are published or not. The documents may come from teaching and research institutions in France or abroad, or from public or private research centers.

L'archive ouverte pluridisciplinaire **HAL**, est destinée au dépôt et à la diffusion de documents scientifiques de niveau recherche, publiés ou non, émanant des établissements d'enseignement et de recherche français ou étrangers, des laboratoires publics ou privés.

Estimating perturbed stress from 3-D borehole displacements induced by fluid injection in fractured or faulted shales

Yves Guglielmi,¹ Christophe Nussbaum,² Jonny Rutqvist,¹ Frédéric Cappa,^{1,3,4}
 Pierre Jeanne¹ and Jens Birkholzer¹

¹Lawrence Berkeley National Laboratory, Energy Geosciences Division, Berkeley, CA 94720, USA. E-mail: YGuglielmi@lbl.gov

²Federal Office of Topography, Swisstopo, Seftigenstrasse 264, CH-3084 Wabern, Switzerland

³Université Côte d'Azur, CNRS, Observatoire de la Côte d'Azur, IRD, Géoazur, Nice, France

⁴Institut Universitaire de France, Paris, France

Accepted 2020 March 2. Received 2020 February 21; in original form 2019 September 7

SUMMARY

Hydrofracturing stress measurements in fractured and anisotropic shales are notoriously difficult, because opening of existing geological features tends to prevent the creation of a pure hydraulic fracture perpendicular to the least compressive principal stress. Here we show how adding 3-D borehole-displacement measurements while conducting the hydraulic injection test helps to better constrain the principal stress orientations and magnitudes. We developed a 3-D fully coupled hydromechanical numerical model to analyse the displacement, fluid pressure and injection flow-rate data measured during an injection pressure-step-rate test conducted to activate a faulted borehole interval in the Mont Terri Opalinus Clay (Switzerland). We find that injected fluids can only penetrate the fault when it is at or above the Coulomb failure pressure. Borehole displacement orientations are sensitive to a $\sim 15^\circ$ variation in the stress-tensor orientation and a 1 MPa stress magnitude variation. Although some dispersion occurs while rupture is propagating along the fault plane ~ 4 m away from the borehole, the maximum density of displacement orientations consistently informs about the stress orientation. Thus, an extended injection step-rate approach coupled with an accurate *in situ* measurement of the borehole wall displacements can be used to better constrain the local stress field perturbations in fractured shales and in heterogeneous rock in general.

Key words: Fault zone rheology; Fracture and flow; Geomechanics; Downhole methods.

1 INTRODUCTION

Stress tensor characterization in and near fracture or fault zones is extremely difficult to conduct, and it is even harder to evaluate the temporal and spatial variation of the stress tensor during fault activation. The most commonly used stress tests, leak-off test (LOT) or hydrofracturing tests (HF), provide just the magnitude and orientation of the minimum principal stress (Zoback *et al.* 2003). Moreover, the tests are usually conducted in intact rock borehole intervals, at distances from fault zones where the influence on the estimated regional stress may eventually be detected from anomalies in the stress profiles (Hickman & Zoback 2004). Another method, called HTPF (hydraulic test on preexisting fractures), allows estimating stresses from the hydraulic stimulation of naturally fractured borehole intervals (Cornet & Valette 1984). This method uses a single borehole where multiple fractures of different orientations are successively isolated with a double packer system and hydraulically tested. A statistical inversion of the different tests allows for an estimation of an average stress tensor for all the tested fractured borehole intervals (Cornet & Valette 1984; Haimson & Cornet 2003). Estimating

stresses from the LOT or HF pressure data relies on the hypothesis that a fracture opens parallel to the direction of the least compressive stress (Hubbert & Willis 1957; Warren & Smith 1985; Murdoch 1995). The principal stress directions are derived from the fracture trace on the borehole wall determined after the test using an impression packer or an image logs. In the case of pre-existing fractures intersecting the test interval (HTPF test), the full stress tensor determination from fluid pressure data relies on the determination of six unknown parameters which requires a sufficient number of tests on natural fractures with different orientations. The normal stress applied on these fractures is estimated from the determination of the shut-in pressure on the pressure-time records. The analysis assumes that single natural fractures can be isolated in the rock mass, which is considered homogeneous within the volume of interest (Haimson & Cornet 2003).

The above assumptions for interpretation of HF stress measurement may be problematic, in particular when measurements are performed around fault zones or in fractured, heterogeneous and anisotropic host rock. A number of key factors results in significant uncertainties in the estimated stress field:

(1) the real fracture opening is impossible to measure from pressure data only (Rutqvist *et al.* 2000);

(2) post-test borehole inspections often are inconclusive since no visible trace of reactivation is left;

(3) the complex stress state related to non-vertical maximum principal stress (e.g. a thrust fault regime) may induce complex HF behaviour (Evans *et al.* 1988);

(4) the hydromechanical and frictional properties of pre-existing heterogeneities intersecting the borehole may impact the HF propagation, and a post-analysis of the HF trace might lead to inaccurate conclusions.

All these factors can introduce ambiguities in interpreting the pressure curves into a stress regime (Warpinski & Teufel 1991). This can therefore result in large uncertainties in the estimation of stress into or near fault zones.

Here we use a 3-D fully coupled hydromechanical numerical model to analyse the results from an injection pressure-step-rate test conducted at ~ 300 m depth in the Mont Terri Main Fault zone in Switzerland. A faulted interval in shales was isolated in a vertical borehole using a double-packer probe instrumented with a high-resolution borehole 3-D displacement sensor called the SIM-FIP (Guglielmi *et al.* 2013). To analyse the test data, we develop a fault model based on a simplified fault zone architecture in the distinct element code 3DEC (Itasca Consulting Group 2016) and first simulate the injection as a local sharply elevated fluid pressure in an initially very low permeable fully saturated fault. Assuming an elastic medium and a pressure diffusion conditioned by rupture growth within the fault, we match the calculated with the observed borehole microdisplacements and injection pressure variations during the fault activation. Then, we discuss how displacements at the borehole wall help to assess the local stress tensor orientation and magnitude while the pressurized patch grows in the fault ~ 4 m away from the injection borehole. Our stress estimations are in reasonable agreement with existing values determined from different stress measurement methods tested at the Mont Terri Underground Laboratory. Through our investigations, we show that adding the displacements to the pressure measurements during a hydraulic stress test allows to better constrain the complex fault activation mechanism, improving the estimation of the full stress tensor orientation and magnitude.

2 EXPERIMENT SETTING

The test described in this paper is set at ~ 300 m depth in a vertical borehole drilled across the Mont Terri Main Fault (Fig. 1a), a mature regional fault zone intersected by the galleries of the Mont Terri Underground Research Laboratory (URL) in Switzerland. The Main Fault is a thrust zone 0.8–3 m thick, with a dip-azimuth/dip-angle of $140^\circ\text{--}165^\circ/40^\circ\text{--}65^\circ$. The fault is intersecting the Opalinus Clay layer in which the URL is nested. This test is one of the tests conducted during the Fault Slip (FS) project that aimed at studying the conditions for fault reactivation and leakage in a very low permeability ($\sim 1 \times 10^{-18}$ m²) shale formation (Fig. 1b). High pressure and ~ 1 -to-3-hr-long injection tests were conducted in 0.14 m diameter boreholes, in sealed intervals set at different locations within and outside the fault zone (Guglielmi *et al.* 2017).

The instrument used for the injection test is a SIMFIP borehole probe, which allows simultaneous and high-frequency measurement of fluid pressure and borehole wall 3-D displacements (Guglielmi *et al.* 2013 and 2015, and Figs 1c and d). The test is located 40.6 m below the URL gallery floor, significantly away from the gallery's

excavation damage zone that extends 3–4 m from the gallery wall (Fig. 1b). The injection interval is a 2.4-m-long borehole section isolated between two inflatable rubber packers (marked in Fig. 1 as 40.6 m in borehole BFS2). The interval was set in the fault's fractured damage zone, 3.4 m above the Main Fault slip surface (i.e. a principal surface where most of tectonic deformation is accommodated, Fig. 1b), based on borehole optical logs analysis. It is intersected by 13 subparallel fault planes with dip-azimuth/dip-angle of $130^\circ\text{--}140^\circ/35^\circ\text{--}55^\circ$, and one minor plane $200^\circ/24^\circ$ which is located at the bottom end of the interval where it is stopped by two $131^\circ/35^\circ$ and $135^\circ/40^\circ$ faults (Figs 2a, c and d). The clay is intact above 40.6 m (Fig. 2b). The displacement sensor is anchored across a 2-to-3-cm-thick minor fault, named the 'Injection Fault' that has an average dip-azimuth/dip-angle of $132^\circ/36^\circ$ ('Minor Fault' in Fig. 2). The sensor is a 0.49 m long and 0.1 m diameter aluminum cage instrumented with fiber optic strain gages in six different directions. The cage is clamped on the borehole wall on both sides of the 'Injection Fault' (Figs 2a and b). When it is clamped, the cage is disconnected from the straddle packer system. When discontinuities intersected by the borehole interval are deforming as a result of the fluid injection into the interval, the cage allows for obtaining angle dependent strain measurements, which are used to constrain the axial and radial displacements of the cage upper anchor relatively to the cage lower anchor (Guglielmi *et al.* 2013). The axial and radial displacement range is 0.7 and 3.5 mm, respectively, and the accuracy is $\pm 5 \times 10^{-6}$ m. A compass set on the probe provides the orientation of measurements with a 0.1° accuracy. The injection pressure is measured in the interval, close to the cage, with a 0.001 MPa accuracy. The injection flowrate is measured close to the injection pump at the surface with a 0.5 l min⁻¹ accuracy. A second vertical borehole (BFS-1) is located 3.07 m horizontally from the injection hole to monitor the fluid pressure and displacement variations induced in the fault core during the test, using the same apparatus (Fig. 1b).

The injection test was conducted in the open hole 1 week after drilling. The borehole was initially dry (no flow was detected) before the test. The injection interval was isolated by inflating the packers to a pressure of 3.5 MPa and saturated with water in chemical equilibrium with the rock formation. Initial interval pressure was set at 0.6 MPa in equilibrium with the local fault zone pore pressure. After installation and pressurization of the interval, a time delay of about 30 min was set for the instruments to equilibrate towards the chamber's temperature.

3 EXPERIMENT RESULTS

A detailed description of the hydromechanical response of the whole test sequence is given in Guglielmi *et al.* (2020). Here, we focus on the pressure test conducted step-by-step with an engine pump (Fig. 3). This test is interesting because when the injection pressure reached the maximum of 5.43 MPa at 573.5 s, the injection pressure stayed constant for about 10 s, followed by a sudden pressure drop, which in turn was followed 20 s after by a rapid and intense pressure increase in the monitoring hole, indicating that a hydraulic connection has been established. The hydraulic connection shows that the radius of influence of the fluid pressure within the fault is at least ~ 3 m, which is the distance between the two boreholes. There is a strong flowrate increase (Fig. 3a) and a radial and axial borehole displacement evolution that highlight the opening of some geological features in the interval (Fig. 3b). When pressure is stepped down to the initial interval pressure, a significant irreversible displacement is

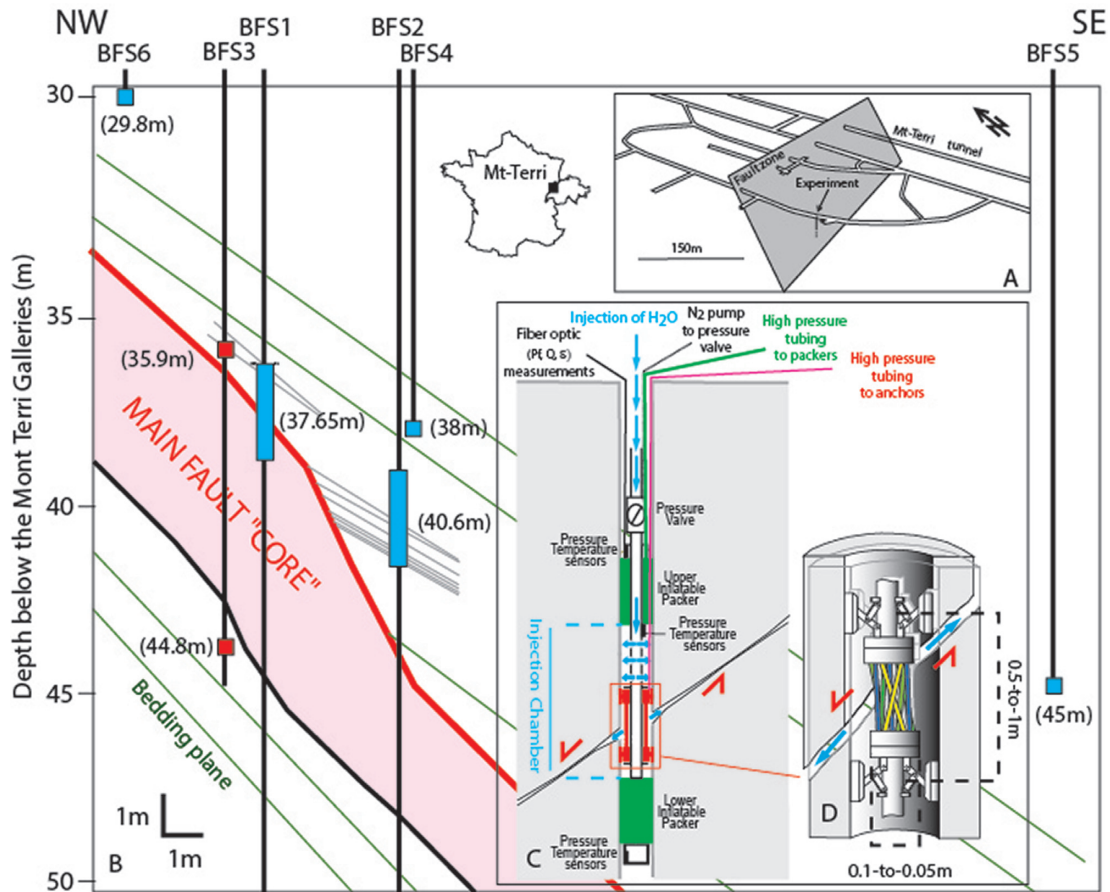


Figure 1. (a) Schematic view of the test location in the Mont Terri underground research laboratory. (b) Geological vertical cross section showing the injection and monitoring intervals location in the fault zone (main fault core is in red, main fault principal shear zone is figured as the thick red line, bedding planes are in green, and fractures/minor faults are in grey, injection and monitoring intervals are in blue in boreholes BFS2 and BFS1, respectively). (c) SIMFIP probe. (d) Borehole wall displacement sensor set in the injection interval of the SIMFIP probe.

observed on both axial and radial components, respectively of -6.5 and -74.7 μm , highlighting that some inelastic fracture activation has occurred (Fig. 3b). A video inspection after the test did not show new fractures, eventually ‘by default’ indicating that some natural fractures intersecting the borehole interval had been reactivated and accumulated damage during the initial pre-slip stage.

Fig. 4 shows details of the injection borehole radial and axial displacements during the 20 s following the onset of the pressure drop. The 1.21 MPa pressure drop is associated with a flowrate increase from 0-to-33.5 l min^{-1} (Fig. 4a). The axial displacement is about four times less than the radial displacement with maximum values of 6 and 22×10^{-6} m at 22 s, respectively (Fig. 4b). Fig. 4(c) shows a stereographic plot of displacement vectors (a displacement vector is defined by two positions of the sensor at 0.1 s time interval). Displacement orientations follow the following plunge-azimuth/plunge-angle trends with time during the pressure drop:

(1) During the first second of the pressure drop (red points in Fig. 4), displacements trends are $325^{\circ}\text{--}N350^{\circ}/25^{\circ}\text{--}50^{\circ}$. During this period, flowrate remains equal to zero.

(2) From 1 to 4.7 s of pressure drop (grey points in Fig. 4), displacements trend migrates from $30^{\circ}/12^{\circ}$ to $70^{\circ}/35^{\circ}$. At the end of this period, the increase of the flowrate and displacements have reached ~ 50 per cent of their maximal value.

(3) After 4.7 s of pressure drop, displacements oscillate from $100^{\circ}/0^{\circ}$ to $140^{\circ}/50^{\circ}$. It corresponds to a period of slow displacements (indeed variations are small, close to the 5 μm resolution of the instrument).

The comparison of the displacement orientation with the interval fracture orientation (green traces and points in Fig. 4c) shows that, during the first second of pressure drop, displacement vectors plot close to the poles of the fractures (green points), meaning that the pressure drop initiates with a dominant opening of the pre-existing planes. With water progressively flowing into the planes (grey and black points), the vectors migrate on or close to the traces of the fracture planes (green circular arcs), meaning that displacements rotate to directions subparallel to the planes. This suggest a dominant reopening of existing fault(s) then evolving into a complex dilatant slip, corresponding to a normal fault activation. Between 8 and 10 s, there is an acceleration in displacement associated to a small increase in fluid pressure and flowrate. It corresponds to a group of 6-to-7 vectors that plot on the green fault traces in the stereogram in Fig. 4(c). Thus, this acceleration may be due to a pure frictional response of the activated fault. Flow rate curve in Fig. 4 also shows that before the triggering pressure of 5.43 MPa, no flow is measured. This means that fluid flow can occur only if this complex mixed mode opening and slipping of the fault(s) is occurring.

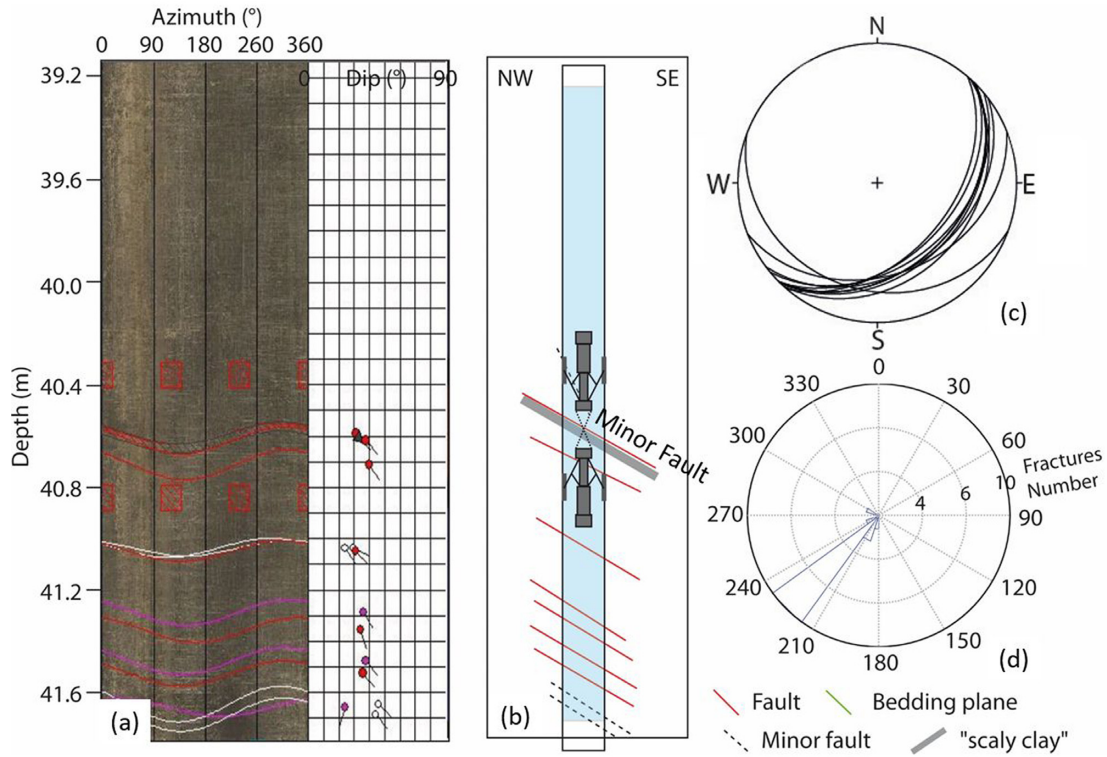


Figure 2. (a) Optical log of the injection interval. (b) Schematic geological structure of the interval with the displacement sensor's location. (c) Stereographic lower hemisphere plot of the interval fractures. Rose diagram of the interval fractures orientations.

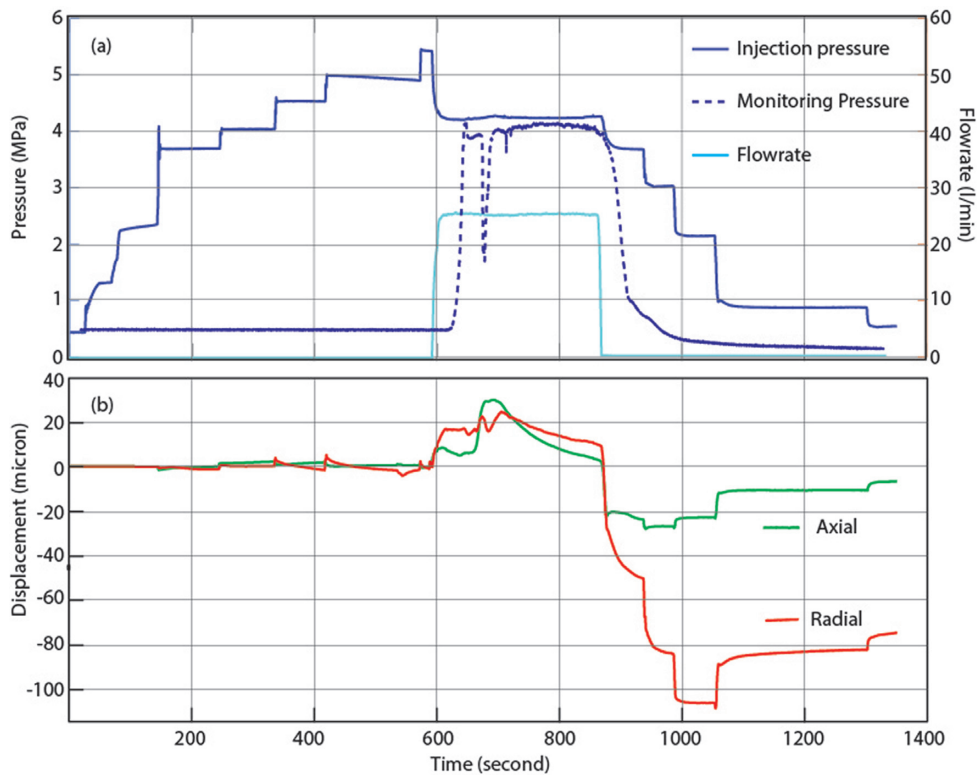


Figure 3. (a) Fluid pressure and flow-rate variations as a function of time at the injection and monitoring intervals during the step-rate test. (b) Borehole wall axial and radial displacement variations as a function of time (it is the displacement of the upper anchor of the sensor relative to the lower anchor considered fixed).

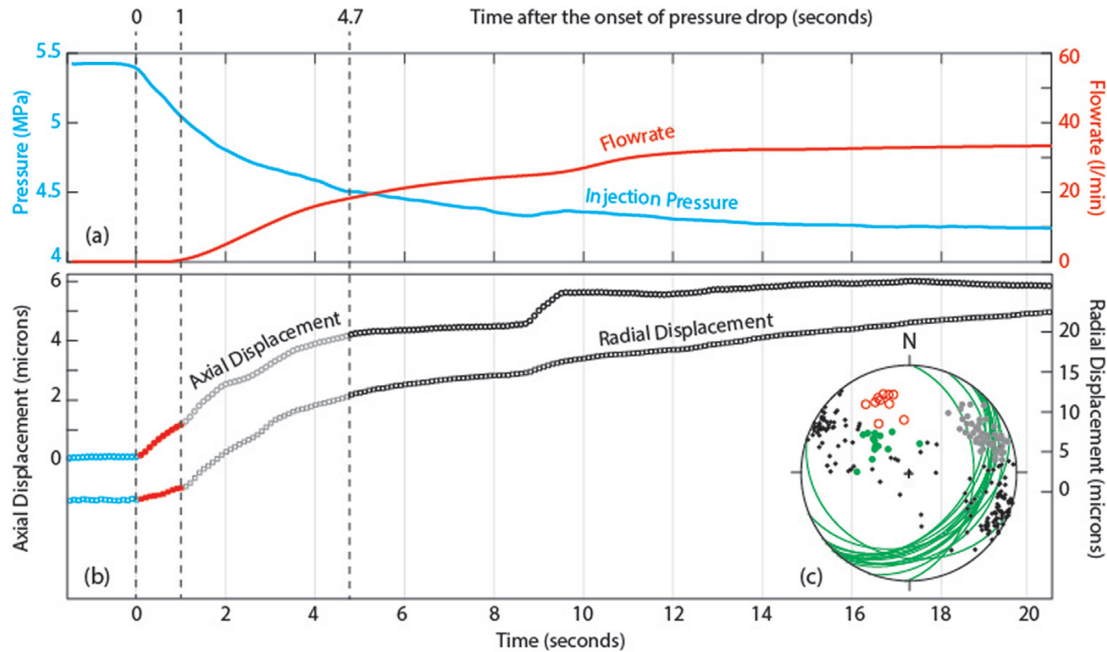


Figure 4. Details of the activation period at the injection interval. (a) Injection pressure drop and flowrate increase during the first 20 s of the fault activation. (b) Axial and radial borehole wall displacements. (c) Stereographic projection of the displacement vectors. Colours of the points are the same in the graphs and in the stereoplot (lower hemisphere projection). Green arc circles figure the injection interval fractures. Green points are the poles of the fractures.

4 NUMERICAL ANALYSES OF STRESS ORIENTATIONS AND MAGNITUDES

4.1 Description of the modelling tool and procedure

We developed a 3-D model of a simplified fault zone architecture using the distinct element code 3DEC (Itasca Consulting Group 2016), which allows conducting fully coupled hydromechanical analyses of the fault movements induced by the injections (Guglielmi *et al.* 2015). The model includes the two boreholes BFS-1 and BFS-2 measuring points (Fig. 5a). The first aim of the modelling is to estimate how adding downhole displacement monitoring during a hydraulic stress test can help improve the full stress tensor estimation in a naturally fractured interval close or within a fault zone. We use a fully coupled hydromechanical approach to best figure the effects of the sharp pore pressure profile evolution from the injection point which is considered as a key parameter driving rupture growth into the fault (Rutqvist *et al.* 2000; Garagash & Germanovich 2012; Viesca & Rice 2012).

The model domain has side-lengths of 20 m and contains three fault families representing the average dip-azimuth/dip-angle of the fault families intersecting the BFS-1 and BFS-2 intervals, respectively $140^{\circ}/60^{\circ}$ (red in Fig. 5a), $129^{\circ}/37^{\circ}$ (yellow in Fig. 5a) and $220^{\circ}/25^{\circ}$ (grey in Fig. 5a). The faults are located in this model, which simplifies the reality according to their approximate location in the field.

We assume that the complex opening of the fault observed in the field corresponds to a fault rupture described by a generalized Coulomb failure criterion. However, because in the field, fluid flow only occurs through the fault after the opening has occurred, our model allows for fluid flow only through the ruptured (either in shear or tension) parts of the fault plane. The injection is applied in a local point source in the middle of the $129^{\circ}/37^{\circ}$ ‘Injection Fault’ (Injection source on the yellow fault in Fig. 5a), and pressure increases in a few subcontacts (i.e. triangular mesh elements) that

figure an initially 0.2 m radius ruptured circular patch. Outside this circular patch, subcontacts must rupture for flow to propagate into the fault zone. When a fault element is ruptured, fluid flow is calculated with the modified cubic law to account for the stress-dependent permeability.

The fault properties used in the model are given in Table 1. The host rock is assumed to be linear elastic with transversely isotropic properties to account for the Opalinus clay bedding. We used the average values at the Mont Terri URL (Bock 2009). The host rock is considered impermeable, which is reasonable considering the very low permeability of Opalinus Clay ($\sim 1 \times 10^{-18} \text{ m}^2$) and the relative short time frame of these experiments. Fault stiffness (K_n , K_s) are estimated to $\sim 100 \text{ GPa m}^{-1}$ based on the ratio between the intact rock Young’s modulus and the thickness of the injection fault. Fault initial permeability, static friction angle and dilation angle were set to $8 \times 10^{-17} \text{ m}^2$ (Jeanne *et al.* 2018), 18 -to- 24° and 11° , respectively, according to average values from laboratory shear tests on Opalinus Clay reconstituted fault gouge samples (Thoeny 2014; Bakker 2017; Orellana *et al.* 2018).

To estimate the stress field, we first considered a lithostatic stress of 7.3 MPa assuming a 290 m overburden and a 2500 kg m^{-3} rock density. In accordance with the observed fault reactivation mechanism, we considered a normal fault regime, meaning that the vertical stress is close to the value of the maximum principal stress. Given the friction coefficient considered in the model, it gives a pre-estimated minimum horizontal stress a factor ~ 0.5 of the vertical stress. The vertical, maximum and minimum horizontal stresses were applied to all the model boundaries (Fig. 5a). An initial fluid pressure of 0.6 MPa was set in the fault(s) in accordance with fluid pressure measurements recovered by piezometres set 5-to-15 m away in the fault zone for the purpose of the experiment (see location in Fig. 1b). The field injection is simulated by applying a step-by-step pressure increase at the model’s fault grid point coordinates (0, 0, 0) (black curve in Fig. 5d) that theoretically represents the measured time-history of pressure imposed in BFS-2 during the *in situ* experiment.

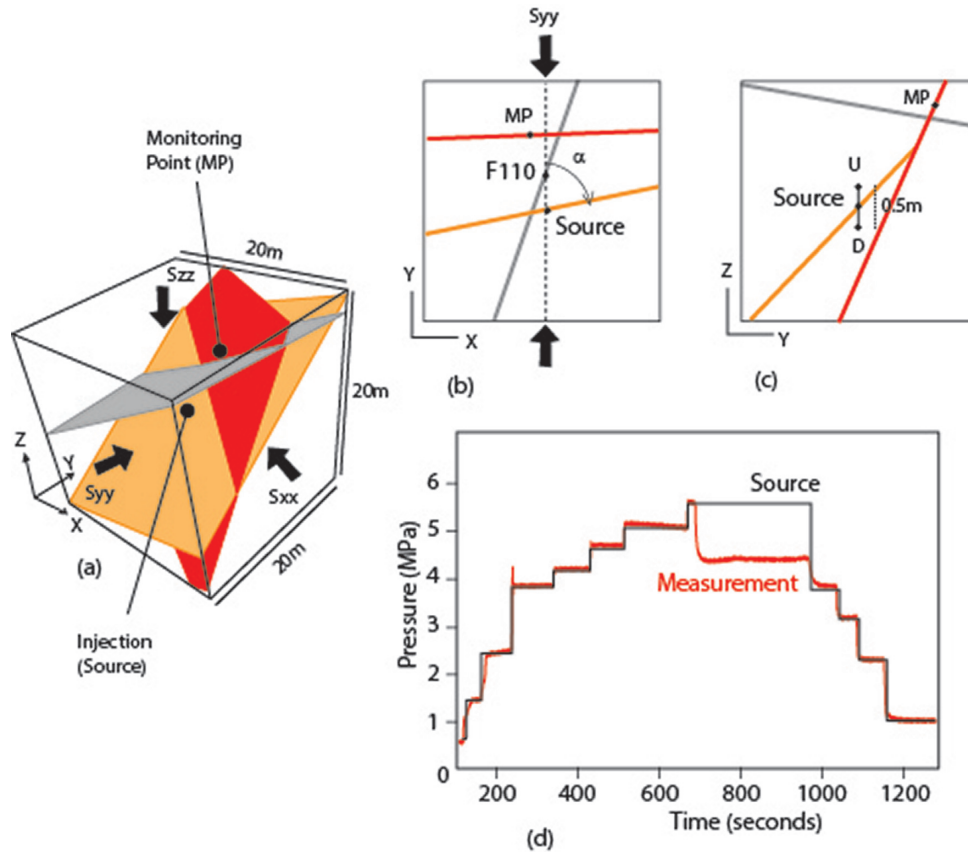


Figure 5. 3DEC numerical model setting. (a) 3-D view of the model geometry; (b) horizontal plane view; (c) vertical plane view; (d) imposed pressure history (black line) at the injection source in the centre of the model. The theoretical black curve reproduces the main shape of the fluid pressure measured *in situ*.

Table 1. Boundary conditions and material properties for the numerical model.

Model size: 20 m × 20 m × 20 m
Stress Boundary conditions:
$\sigma_x = -3.8 \times 10^6$ Pa, $\sigma_y = -4.7 \times 10^6$ Pa, $\sigma_z = -5.5 \times 10^6$ Pa
Initial pore pressure: $p_p = 0.5 \times 10^6$ Pa
Properties of the intact rock: Elastic constitutive model
Density: $\rho = 2500$ kg m ⁻³
Young's modulus parallel to bedding: $E_1 = E_2 = 7.2 \times 10^9$ Pa
Young's modulus normal to bedding: $E_3 = 2.8 \times 10^9$ Pa
Poisson's ratio parallel to bedding: $\nu_{12} = 0.24$
Poisson's ratio normal to bedding: $\nu_{13} = \nu_{23} = 0.33$
Shear modulus parallel to the bedding: $G_{12} = 2.9 \times 10^9$ Pa
Shear modulus normal to the bedding: $G_{13} = G_{23} = 1.2 \times 10^9$ Pa
Properties of the faults: Mohr–Coulomb constitutive model
Normal stiffness: $K_n = 100 \times 10^9$ Pa m ⁻¹ = $\frac{E_3}{2.8 \times 10^{-2}}$
(2.8×10^{-2} m is the injection fault thickness estimated from borehole cores)
Shear stiffness: $K_s = 100 \times 10^9$ Pa m ⁻¹ $\sim K_n$
Friction angle: $\phi = 22^\circ$ and Dilation angle: $\varphi = 11^\circ$
Cohesion: $c = 0.5 \times 10^6$ Pa
Tensile strength: $j_{\text{tens}} = 0.5 \times 10^6$ Pa
Hydraulic aperture at zero normal stress: $a_{\text{zero}} = 6 \times 10^{-5}$ m
Maximum hydraulic aperture: $a_{\text{max}} = 1 \times 10^{-3}$ m
Residual hydraulic aperture: $a_{\text{res}} = 2 \times 10^{-7}$ m
Fluid properties:
Bulk modulus: $K_f = 2 \times 10^9$ Pa
Density: $\rho_f = 1000$ kg m ⁻³
Dynamic viscosity: $\mu = 1 \times 10^{-3}$ Pa.s

Injected flowrate is then calculated at the same point. Displacements (U_x , U_y , U_z) of the fault-hanging wall towards the footwall are calculated at the injection point, as well as fault pressure at the monitoring point (Figs 5b and c).

First, the model is run to equilibrium to establish the initial static stress and pressure conditions. Then, the injection pressure is applied step-by-step (Fig. 5d). The principal stresses azimuth is incrementally rotated of an angle ' α ' until a best match between calculated and measured displacements orientation, and the principal stresses magnitudes is varied until fault opening pressure is obtained both at BFS-1 and BFS-2 (Figs 6 and 7). We then conduct a numerical study of fault displacements sensitivity to stress orientation to estimate the accuracy of our modelling approach (Fig. 8).

4.2 Modelling results

4.2.1 Best-fitting solution

Fig. 6 shows the model solution that reasonably matches measured displacements, fault opening pressure and flow-rate variations with time. We did not attempt to make an exact match of simulated and observed data but rather tried to obtain a reasonable agreement to the general evolution and magnitude of data presented in Fig. 6. Consequently, we did not simulate each stage of accelerated and decelerated displacement and pressure because our study mainly focuses on the estimation of the static stress field. The best-fit solution is obtained for a state-of-stress with values of $\sigma_v = 5.5$ MPa, $\sigma_H = 4.7$ MPa, oriented N310 subhorizontal, and $\sigma_h = 3.8$ MPa, oriented N040 subhorizontal (Table 2). The model calculates no flow until the pressure is raised to 5.43 MPa, a value that corresponds, in accordance with measurements, to a sharp flowrate increase followed several seconds later by a pressure increase at the monitoring point. At 618 s when pressure is maximum at the monitoring point (green curve in Fig. 6a), the calculated radius of the pressurized patch in the fault is about 4 m. The general evolution of the radial and axial displacements at 5.43 MPa is reasonably reproduced by the model (Figs 6b and c).

In details, during pressure steps with injecting pressure below 5.43 MPa there is a small step-increase of the calculated displacements related to the fault elastic response to pressure step increases. This is poorly reproducing the measurements, which display a much more complex response characterized by (1) a larger magnitude variation when pressure is increased from one step to the next one and (2) a transient decrease-versus-time while pressure is held constant during the steps. This is observed above ~ 3.5 MPa. This difference between the model and the measurements highlights that either (case 1) some failure initiates at a pressure lower than 5.43 MPa, but with no significant fluid penetration into the fault, or (case 2) that elastic opening of the fault and limited pressure diffusion into matrix rock produce the observed time-dependent displacements. In case 1, given the low amount of injected fluid (not measurable during the test), if failure occurs, it is local. In the model, it is not propagating away from the 0.2 m radius initial ruptured circular patch considered to figure the injection source. In case 2, the model does not reproduce pressure diffusion in the matrix, which is assumed impermeable. When pressure increases from 4.9 to 5.43 MPa, there is an immediate calculated radial displacement followed by a rebound during ~ 10 s, and finally a transient increase while the rupture propagates within the fault towards the monitoring point (Fig. 6c). The calculated immediate radial response overestimates

the measured one, although the maximum amplitude and shape of the radial displacement curve reasonably reproduce the experimental one. The calculated axial displacement variation shows a ~ 20 s delay in good agreement with measurement (Fig. 6b). It occurs during the injection pressure drop (Fig. 6a). In Figs 7(a) and (b), we show details of the displacements calculated normal (opening) and parallel (slip) to the fault plane during the 60 s following the onset of the rupture. As a matter of comparison, Figs 6(b) and (c) were previously showing the displacements calculated ~ 0.3 m away from the fault, corresponding to the 'exact' location of the sensor relative to the fault in the field (see Fig. 2 for location). Fig. 7(a) is thus our best estimate of the fault opening and shear displacement deduced from the model of the best fit to experimental data. The first ~ 30 s of rupture display a larger normal opening compared to slip on the fault. Slip is progressively increasing with time while most of the opening at the injection point occurs during the first 10 s. During the first second of failure, the calculated orientation of the displacements in Fig. 7(d) matches well with the measurements corresponding to the red points in Fig. 7(c). While rupture is propagating, we observe a scattering of the calculated displacements in Fig. 7(e) (black points). This scattering can also be visualized using the plot of the vector density per 1/50 area of the stereographic circle (Figs 7f and g). It shows two areas with a maximum density >25 vectors/area: a large one which is in the NW quadrant of the stereogram corresponds to displacement vectors displaying a high angle ($>60^\circ$) with the fault plane and a small one which is in the southeastern quadrant corresponds to vectors displaying a low angle ($<15^\circ$) with the fault plane. In the model, such a dispersion of the calculated displacements is explained by the dominant dilatant opening compared to slip on the fault at the injection point. However, our analysis provides a reasonable evaluation of field data.

4.2.2 Sensitivity to stress tensor orientation

Fig. 8 shows stereo-plots of the density of calculated displacement vectors for different numerical models where the horizontal stresses were rotated with increments $\alpha = 20^\circ$ assuming the best-fitting model geometry and properties. In all the models, the stress magnitudes are the same. The number of displacement vectors ' n ' is also about the same between models, respectively of 1200–1950. We also compare our fully coupled numerical model with a more simple calculation of the effective maximum shear stress on the injection plane by entering the tensor value and the pressure at failure (5.43 MPa) using the MohrPlotter open source software [R. W. Allmendinger©]. This approach is assuming that pressure at failure applies homogeneously in the entire fault plane. Pressure heterogeneity related to the complex fluid penetration with rupture propagation in the fault is not considered. The result is a unique vector figured as the black point located on the fault plane in the stereograms (Fig. 8). Given the relative simplicity of the interval geology (one single fault family with smooth surface characteristics, Fig. 2), we hypothesize that this approach should be a reasonable proxy to slip estimation on the activated plane.

When minimum horizontal stress σ_h is N320, corresponding to the case where the fault is the most favourably oriented to fail in shear (i.e. critical failure case), the maximum density of displacement vectors calculated with the fully coupled model perfectly matches with the slip vector calculated with the Mohr-Plotter model. In addition, there is little scattering of the vectors around the slip

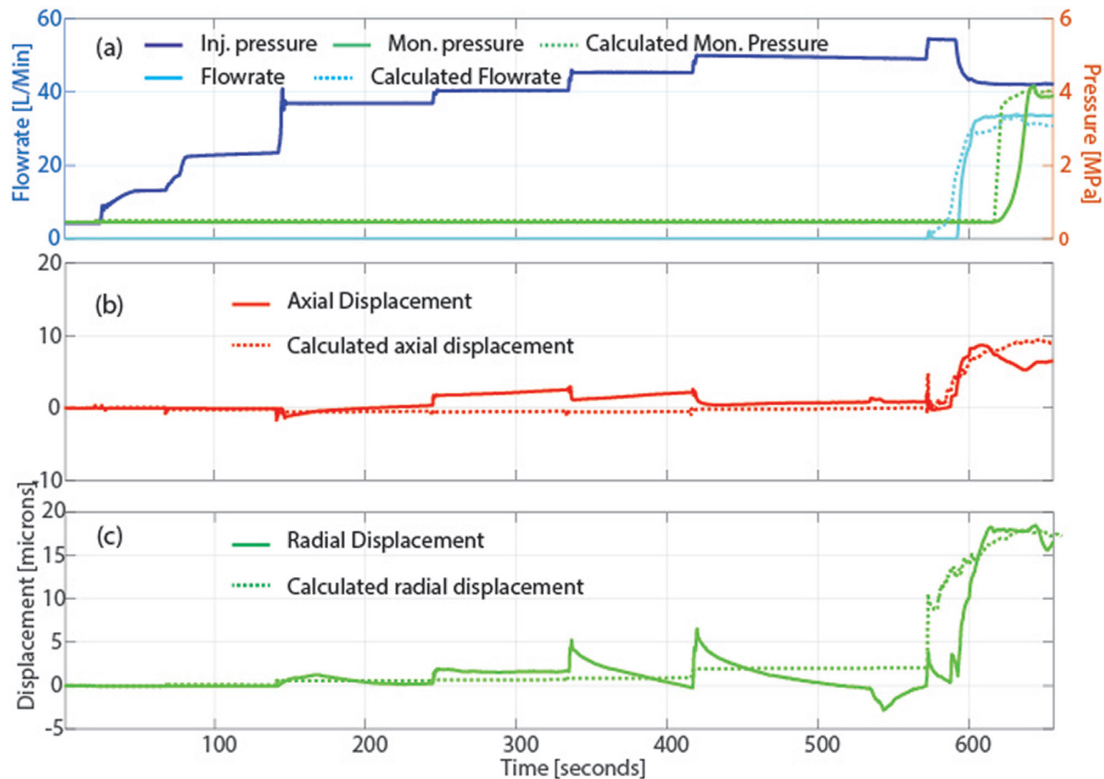


Figure 6. Best-fitting solution between calculated (dashed lines) and measured (solid lines) (a) pressures and flowrate, (b) axial and (c) radial displacements.

vector. This is in good accordance with the theory assuming that the shear stress direction on any fault plane corresponds to the slip direction (Gephart 1990). Deviation between the maximum density of displacement vectors and scattering of vectors orientation both increase with the deviation of σ_h from the critical failure case. The case σ_h N060° illustrates a particularly unfavourably oriented case for the fault to fail in shear. Displacements clearly scatter outside the fault trace. In such a case there is a low potential for the fault to fail in shear. Nevertheless, in all other cases, there are two maximum density zones showing that opening and slipping modes coexist during the fault reactivation.

5 DISCUSSION

5.1 Effect of heterogeneity on hydraulic based stress measurement in fractured shales

The Mont Terri is an interesting example where hydraulic fracturing has shown little success in meeting the criteria for using the method for stress measurements in strongly anisotropic shales. Indeed, the method most exclusively induced the reactivation of bedding planes (or/and) fractures in Opalinus clay (Doe & Vietor 2015). Same thing is observed in the test described in this paper. Our interpretation of the complex reactivation of a bedding parallel fault shows that conditions do not appear favourable to create a new vertical fracture perpendicularly oriented to σ_3 . First reason might be that the horizontal stress values are relatively close to each other, driving a relatively low hoop stress concentration, which cannot exceed the strength of the rock. Using Hubbert & Willis (1957) criteria, we can estimate the fracture pressure $P_b = 3 \times \sigma_h - \sigma_H + T - P_0 = 8$ MPa (T is the intact rock tensile strength equal to ~ 2 MPa and P_0 the formation pore pressure equal to 0.5 MPa, $\sigma_h = 3.8$ MPa, $\sigma_H = 4.9$ MPa).

This fracture pressure value is significantly larger than the fault opening pressure of 5.43 MPa. Another reason for the lack of a vertical fracture intersecting the bedding planes and or the fault-parallel-to-bedding is that several authors (Amann *et al.*; Thoeny 2014) showed that tensile and cohesive strengths of such structures are dramatically low, respectively ~ 0.5 and 0.6 MPa, which make these planes much weaker than the intact rock.

We calculated that fault is opening when the injection pressure induces a drop to almost zero of the normal stress on the fault(s). This is consistent with previous theoretical studies that demonstrated that a local fluid pressure must get close to the total fault normal stress before a fault slip being triggered (Viesca & Rice 2012). One reason is that an elevated fluid pressure is required to activate the fault which is unfavourably oriented towards stress as described in different previous theoretical works (Axen 1992; Rice 1992; Faulkner & Rutter 2001; Garagash & Germanovich 2012). In addition to that, we find that in such a shale fault, this effect is amplified by the initial very low initial permeability of the fault and by the low rigidity of the rock surrounding the fault. This is creating conditions for a mixed opening and shearing rupture mode of propagation. Indeed, fluid needs to force its way through ruptured patches within the fault. Result is an exceptionally high normal displacement measured at the injection point compared to the fault tangential displacement.

5.2 Comparison with other stress tensor estimations at Mont Terri

Here we compare our estimated stress tensor with previous tests conducted at the Mont Terri URL. The stress tensor has been estimated at different locations in the Mont Terri Laboratory through three different types of measurements: (1) slotter probe utilizing a

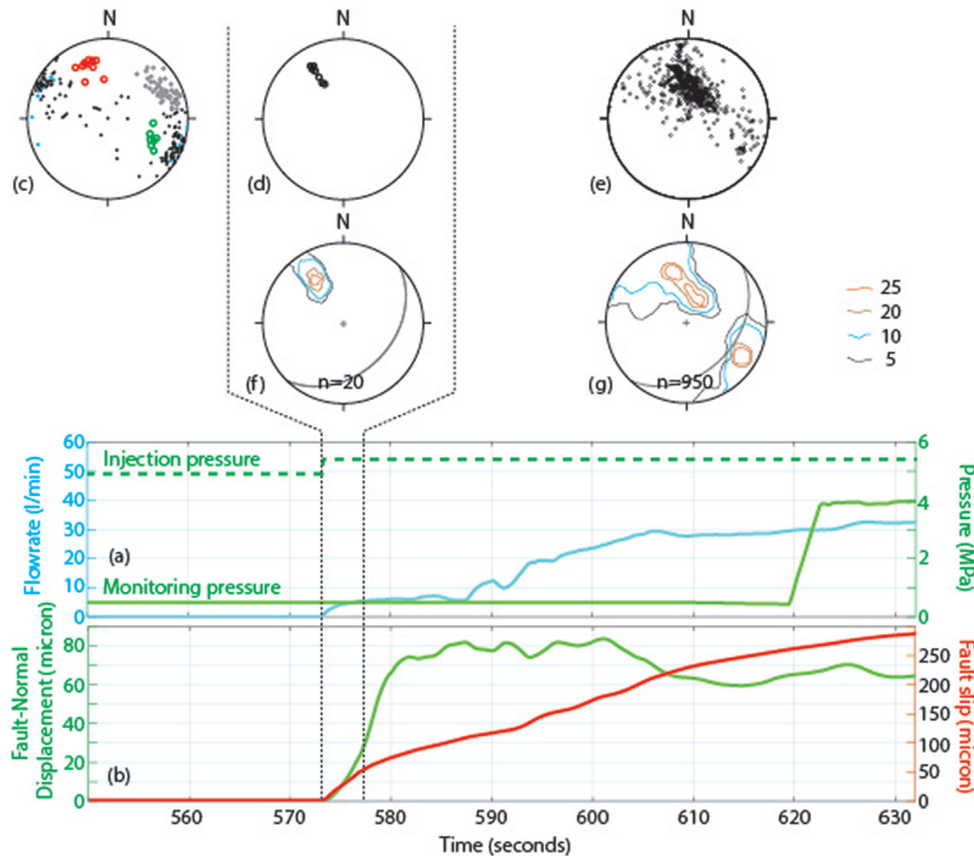


Figure 7. (a) Details of calculated fault pressure at injection (dashed green line), monitoring (continuous green line) and flowrate (cyan continuous line) during the first minute of activation. (b) Calculated fault normal opening and slip. (c) Measured displacement vectors in a stereographic projection (lower hemisphere). (d) Calculated displacement vectors after 1 s of pressure drop. (e) Calculated displacement vectors after 1 min of pressure drop. (f) Density plot of displacement vectors (density = number of vector per 1/50 area of the stereo sphere, n is the total number of vectors). (g) Density of displacement vectors after 1 min of pressure drop.

strain relief testing method (Bock 1993); (2) undercore method using the CSIRO triaxial strain cells and (3) HF (Haimson & Fairhurst 1970). The results from all these measurements are discussed in several technical notes (Martin & Lanyon 2003; Corkum & Martin 2007; Doe & Vietor 2015). The following ‘synthesized’ value at the depth of the URL’s galleries is characterized by the following total principal stresses, $\sigma_1 = 6\text{--}7$ MPa subvertical to $N210\text{--}70^\circ$ plunge, $\sigma_2 = 4\text{--}5$ MPa $N320^\circ$ subhorizontal to 7° plunge, and $\sigma_3 = 0.6\text{--}2.2$ MPa $N052^\circ$ subhorizontal to 18° plunge. At the location of our test which is roughly in the middle of the Opalinus Clay layer, the greatest uncertainty is the magnitude of σ_3 which appears low compared to the pore pressure of about 2 MPa measured away from the galleries excavation damage zone. For these reasons, other authors recently re-estimated σ_3 to higher values of 2.5-to-2.9 MPa (Amann *et al.* 2018). In addition, the hydraulic tests allowed for a good estimate of the stress magnitude normal to the bedding, estimated to be 4.2 MPa. Uncertainty ranges for the orientation of the principal stresses have not been clearly estimated. The slight plunge of σ_1 and the low σ_3 value could be related to a topographic effect due to a deep valley to the South West of the Mont Terri laboratory site. Finally, most of the stress estimations were done at the galleries level. There is a limited (and unpublished) number of stress measurements at the depth of the experiment which is ~ 40 m below the galleries. These tests tend to show higher values up to 3.9 MPa for σ_3 at 50 m depth below the galleries (Doe & Vietor 2015). Table 2

shows a summary of the range of values for the reference Mont Terri stress tensor.

Fig. 8 and Table 2 show that our best fit reasonably plots within the uncertainty range of the Mont Terri tensor estimated by other methods. Indeed, the orientation of the calculated displacements are highly sensitive to the orientation of the stress tensor during the first 20 s of pressure drop. Approximating the maximum vector density area (red line in Fig. 8) to a circle gives an estimated $\sim 10^\circ$ resolution of the displacement orientation and dip angle calculated with the hydromechanical numerical approach. The resolution also depends on the orientation of the activated fault, which can be picked on borehole image logs with an error of $\sim 5^\circ$ on both dip and dip direction. Thus, the resolution on the stress orientation is estimated to $\sim 15^\circ$.

5.3 Representativeness of stress estimations away from the borehole

Thanks to the hydraulic connection between two measuring points, it was possible to estimate the hydraulic diffusivity of the fault zone and a radius of the fault activation patch of about 4 m. This is related to several orders of magnitude permeability variation, which are consistent with other observations in faulted shales (Cuss *et al.* 2011; Guglielmi *et al.* 2015). We estimate a pressure patch growth velocity of ~ 0.08 m s^{-1} during which fluid flows into the fracture from the wellbore faster than it does into the wellbore from the

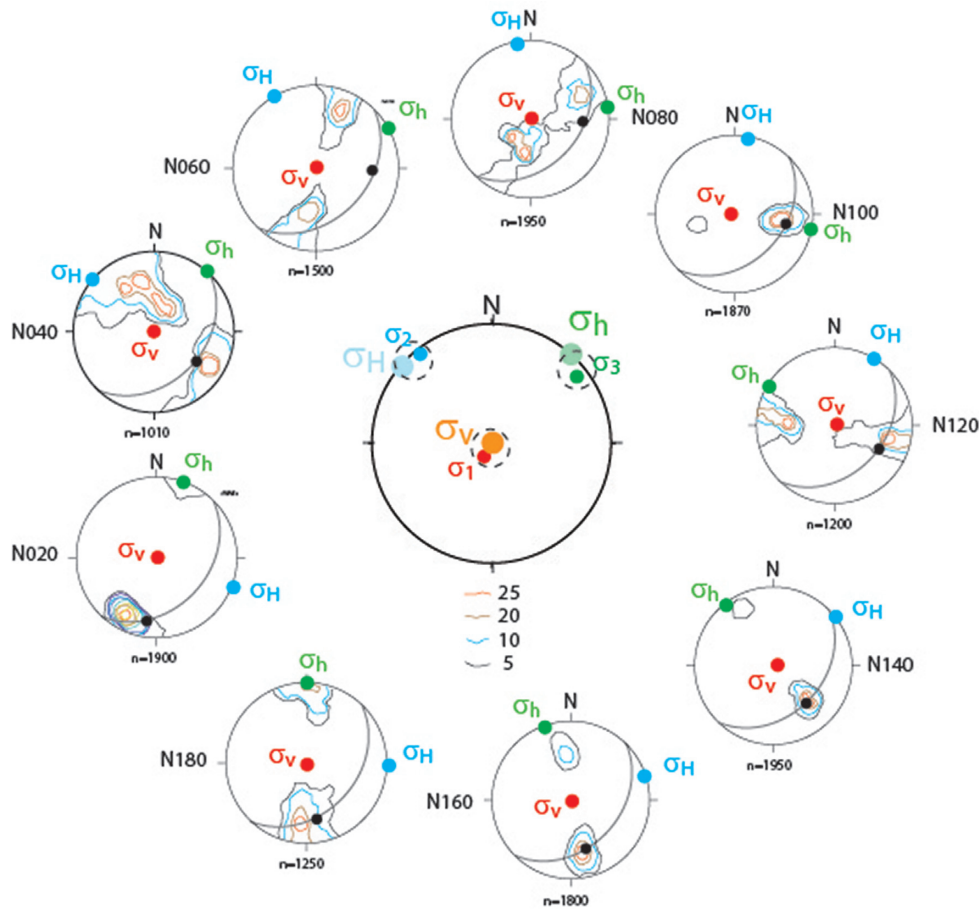


Figure 8. Small stereo circles show the density of displacement vectors for different minimum horizontal stress orientations applied to the numerical model boundaries (n is the total number of vectors). The black arc circle figures the injection fault plane considered in the model. The black point is the maximum shear stress vector calculated on the plane using the Mohr-Plotter software. The large stereo circle in the middle compares the best fit solution which is figured as the large light coloured points (size of the points is the accuracy of the determination) to the stress tensor average value (small points) and range of variations (dashed line black circles) estimated by previous works in the same zone of the Mont Terri URL.

Table 2. Stress tensor at Mont Terri (upper lines) and tensor estimated in this study (lower lines).

Mont Terri stress tensor (range of values from the literature)			
	Stress magnitude (MPa)	Dip direction	Dip
σ_1	6-to-7 (6.5)	210°	70°-to-90° (80°)
σ_2	4-to-5 (4.5)	310°	0°-to-7° (3.5°)
σ_3	0.6-to-2.9 (1.8)	52°	0°- to-18° (9°)
Stress tensor estimated in this study			
σ_1	5.5 ± 0.1	-	90°
σ_2	4.7 ± 0.1	310° ± 15°	0°
σ_3	3.8 ± 0.1	40° ± 15°	0°

pump. Hence, as it is observed in usual leak-off tests, the pressure drops in the injection chamber. Analysing the displacements continuously monitored during the 20 first seconds of pressure drop gives information on fault rupture behaviour far away from the borehole stress influence (about 50 borehole radii away). The synchronous pressure and displacement measurements demonstrated that the onset of fracture displacement occurs before fluid flows into the fracture. During that ‘dry’ rupture period, the displacement vectors picked at the onset of the pressure drop at the injection point represent a 0.4 m radius rupture zone, already six times larger than the borehole radius and thus reasonably representative of fault rupture away from the borehole influence. Modelling the

20 initial seconds of fault reactivation with a 3-D distinct element approach showed that, although fault displacement orientations are much more scattered during this longer period compared to the first second, the maximum density of displacement vectors still matches reasonably well with the stress tensor’s orientation. Thus, the fully coupled hydromechanical analysis that allows matching both the fault displacement directions and the injected pressure and flowrate proves being able to estimate the representability of the stresses significantly away from the borehole wall. Nevertheless, it is well known that the far field stress magnitudes and orientations may drastically be perturbed in the near field of a fault or a fracture (Lei & Gao 2018).

5.4 Limitations of the approach

The accuracy on our estimations of the orientation and magnitude of the tensor components depends on the characteristics of the numerical model used to calculate displacements at rupture, fluid diffusion and the variation of the full effective stress tensor. The model went through several simplifications:

- (1) the borehole was explicitly discretized in the model.
- (2) fault geology was simplified to a single plane.
- (3) the Mohr–Coulomb criterion was used as a first order approximation to model the rupture of the preexisting natural fault.

As the stress state around a borehole is triaxial, a true-triaxial failure criterion might be more appropriate for obtaining information on the full stress tensor, since the Mohr–Coulomb criterion neglects the effect of the intermediate principal stress (Mogi 2007). Using a Mogi failure criterion (that considers the intermediate stress) in a FEM numerical model, Singh *et al.* (2019) showed that plastic deformation around a borehole was reduced by about 13–20 per cent compared to when using Mohr–Coulomb criterion because the out-of-plane stress increases well bore stability. Intermediate stress effects also appear to depend on the rock type, and anisotropy or weak planes may influence the results. Conducting triaxial tests on highly laminated shales, Ambrose (2014) observed that failure was consistent with the Coulomb criterion for the following range of angle between the direction of σ_1 and the direction of the plane of weakness, $[0^\circ\text{--}10^\circ]$, 90° and $[45^\circ\text{--}75^\circ]$. He identified a mixed failure mode due to competition of shale matrix and weak plane for angles of 10° -to- 35° ; that he interpreted as a transition regime where the intermediate stress should be considered for a better description of failure.

Guglielmi *et al.* (2015) tested the effects of different model properties on fault rupture propagation, respectively the fault normal stiffness (j_{kn}), friction angle (ϕ), hydraulic aperture (b_h) and whether the intact rock is isotropic (reference case) or transversely anisotropic (to figure the bedding's mechanical anisotropy). Result is that properties have minor influence on the plastic vector orientation during the few seconds after fault opening to fluid flow, although friction and hydraulic aperture variations have a significant effect on rupture propagation length and, thus, on the estimation of the radius of influence of the test.

It is thus hard to estimate how accurate the modelling choices made in this study are. The high angle (54°) between the activated plane and σ_1 , the low range of the mean stress (compared to deep borehole conditions) and the drastically weak fault planes that localized the rupture (no new rupture planes were observed at the borehole wall after the test) advocate that, in our case, such a simplified numerical approach is a reasonable first order approximation. The good correspondence of our stress tensor estimation with other estimations done at Mont Terri brings some confidence in the results, although, following the elements exposed in this chapter we may estimate a ~ 1 MPa accuracy of the stress magnitudes.

6 CONCLUSION

We conducted a fully coupled hydromechanical numerical analyses of direct *in situ* borehole wall displacements induced by an injection pressure-step-rate test conducted in a faulted Opalinus Clay interval (Mont Terri), using the distinct element code 3DEC. We observed that the displacements are reasonably well explained by mixed ~ 80 μm opening and ~ 255 μm slip on a prominent fracture zone isolated in the pressure-step-rate test. Our model assumes that the driving

phenomenon is the pressurized water forcing its way within the rupture patch of the activated fracture, following a Coulomb failure triggered by stress concentration at the tip of the pressurized patch. We observe that displacements at the borehole wall are very sensitive to the stress tensor orientation. In addition, we show that the fully coupled hydromechanical modelling approach allows matching a realistic model for the dynamic permeability increase of the ruptured fault and provides estimates for a ~ 4 m hydraulic radius of influence of the test. Although some dispersion in the displacements orientation occurs, the maximum density of displacements orientation still provides very good information on the stresses while rupture is growing away from eventual stress perturbations close to the injection well. We estimate an accuracy of $\sim 15^\circ$ of the tensor orientation and of ~ 1 MPa of the stress values. Interestingly, integrating the displacement measurements in the test and in the analyses allows identifying that the fault activated in response to injection although it being poorly oriented for failure towards stress. Such fault activation behaviour may be typical of the hydromechanical response of very low permeability faulted or fractured shale to a local elevated fluid pressure. Such behaviour may also extend to the activation of bedding anisotropy given some particular stress contexts or some contrasts between anisotropic properties of shales but this remains to be confirmed. Thus, repeating the tests at different interval depths along a borehole should allow a true and direct profiling of the local stresses. It may help characterize the local perturbations of the far field stresses for a better estimation of stimulation efficiency and induced seismicity related to different types of deep fluid manipulations.

ACKNOWLEDGEMENTS

The authors are deeply grateful to the four partners of the Mont Terri Project that contributed to the funding of the FS experiment: the Swiss Federal Office of Topography (Swisstopo), the Swiss Federal Nuclear Safety Inspectorate (ENSI), the Japanese Atomic Energy Agency (JAEA) and the U.S. Department of Energy. The Mont Terri Project is an international research project for the hydrogeological, geochemical, and geotechnical characterizations of a clay formation (Opalinus Clay). Funding for Berkeley Lab's analysis of the FS data described in this study was provided by the Assistant Secretary for Fossil Energy as part of the Core Carbon Storage and Monitoring Research (CCSMR), by the Spent Fuel and Waste Science and Technology - Office of Nuclear Energy and by the National Risk Assessment Partnership (NRAP) programs of the U.S. Department of Energy under contract DEAC02-05CH11231. Experimental data are available in the supporting information. We thank the reviewers for insightful input that improved this paper.

REFERENCES

- Amann, F., LeGonidec, Y., Senis, M., Gschwind, S., Wassermann, J., Nussbaum, C. & Sarout, J., 2018. Analysis of acoustic emissions recorded during a mine-by experiment in an underground research laboratory in clay shales. *Int. J. Rock Mech. Min. Sci.*, **106**(2018), 51–59.
- Ambrose, J., 2014. Failure of anisotropic shales under triaxial stress conditions, *PhD thesis*, Imperial College London, Department of Earth Science and Engineering, 265p. (<https://spiral.imperial.ac.uk> > bitstream > Ambrose-J-2014-PhD-Thesis)
- Axen, G.J., 1992. Pore pressure, stress increase, and fault weakening in low-angle normal faulting. *J. geophys. Res.*, **97**, 8979–8991. 35.
- Bakker, E., 2017. Frictional and transport properties of simulated faults in CO₂ storage reservoirs and clay-rich caprocks, *PhD dissertation*, Utrecht Studies in Earth Sciences, N° 124, ISBN/EAN: 978-90-6266-4481.

- Bock, H., 2009. RA Experiment - Updated Review of the Rock Mechanics Properties of the Opalinus Clay of the Mont Terri URL based on Laboratory and Field Testing, Technical Report TR 2008-04, Mont Terri Project Underground Rock Laboratory, c/- Project Manager Christophe Nussbaum, Geotechnical Institute Ltd., Gartenstrasse 13, CH - 3007 Bern / Switzerland.
- Bock, H.F., 1993. *Measuring In-Situ Rock Stress by Borehole Slotting*, Cambridge.
- Corkum, A.G. & Martin, C.D., 2007. Modelling a mine-by test at the Mont Terri rock laboratory, Switzerland, *Int. J. Rock Mech. Min. Sci.*, **44**, 846–859.
- Cornet, F. & Valette, B., 1984. In situ stress determination from hydraulic injection test data, *J. geophys. Res.*, **89**(B13), 11527–11537.
- Cuss, R.J., Milodowski, A. & Harrington, J.F., 2011. Fracture transmissivity as a function of normal and shear stress: First results in Opalinus clay, *Phys. Chem. Earth*, **36**, 1960–1971.
- Doe, T. & Vietor, T., 2015. DS (Determination of stress) Experiment: Review of In Situ Stress Measurements and Their Context. Synthesis report, Mont Terri Technical Report TR 2012-06. Federal Office of Topography (Swisstopo), Wabern, Switzerland. www.mont-terri.ch
- Evans, K.F., Scholz, C.H. & Engelder, T., 1988. An analysis of horizontal fracture initiation during hydrofrac stress measurements in granite at North-Conway, New-Hampshire, *Geophys. J.-Oxford*, **93**, 251–264.
- Faulkner, D.R. & Rutter, E.H., 2001. Can the maintenance of overpressured fluids in large strike-slip fault zones explain their apparent weakness? *Geology*, **29**, 503–506.
- Garagash, D.I. & Germanovich, L.N., 2012. Nucleation and arrest of dynamic slip on a pressurized fault, *J. geophys. Res.*, **117**, B10310, doi:10.1029/2012JB009209.
- Gephart, W.J., 1990. Stress and the direction of slip on fault planes, *Tectonics*, **9**(4), 845–858.
- Guglielmi, Y., Cappa, F., Lançon, H., Janowczyk, J.B., Rutqvist, J., Tsang, C.F. & Wang, J.S.Y., 2013. *ISRM Suggested Method for Step-Rate Injection Method for Fracture In-Situ Properties (SIMFIP): Using a 3-Components Borehole Deformation Sensor*. Rock Mechanics and Rock Engineering, doi:10.1007/s00603-013-0517-1.
- Guglielmi, Y., Elsworth, D., Cappa, F., Henry, P., Gout, C., Dick, P. & Durand, J., 2015. In Situ observations on the coupling between hydraulic diffusivity and displacements during fault reactivation in shales, *J. geophys. Res.*, **120**, 7729–7748.
- Guglielmi, Y., Birkholzer, J., Rutqvist, J., Jeanne, P. & Nussbaum, C., 2017. Can fault leakage occur before or without reactivation? Results from an in situ fault reactivation experiment at Mont Terri, *Energy Procedia*, **114**(2017), 3167–3174.
- Guglielmi, Y., Nussbaum, C., Jeanne, P., Rutqvist, J., Cappa, F. & Birkholzer, J., 2020. Complexity of fault rupture and fluid leakage in shale: insights from a controlled fault activation experiment, *J. geophys. Res.*, **125**, doi:10.1029/2019JB017781.
- Haimson, B. & Fairhurst, C., 1970. In-situ stress determination at great depth by means of hydraulic fracturing, in *Rock Mechanics—Theory and Practice. The Proceedings of the 11th Symposium on Rock Mechanics*, 16–19 June 1969, Berkeley, pp. 559–584.
- Haimson, B.C. & Cornet, F.H., 2003. ISRM suggested methods for rock stress estimation part 3: hydraulic fracturing (HF) and/or hydraulic testing of pre-existing fractures (HTPF), *Int. J. Rock Mech. Min. Sci.*, **40**, 1011–1020.
- Hickman, S. & Zoback, M., 2004. Stress orientations and magnitudes in the SAFOD pilot hole, *Geophys. Res. Lett.*, **31**, L15S12, doi:10.1029/2004GL020043.
- Hubbert, M.K. & Willis, D.G., 1957. Mechanics of hydraulic fracturing, *Trans. Am. Inst. Min. Metall. Eng.*, **210**, 153–163.
- Itasca Consulting Group, 2016. *3DEC, 3-Dimensional Distinct Element Code*. Itasca Consulting Group.
- Jeanne, P., Guglielmi, Y., Rutqvist, J., Nussbaum, C. & Birkholzer, J., 2018. Permeability variations associated with fault reactivation in a claystone formation investigated by field experiments and numerical simulations, *J. geophys. Res.*, **123**(2), 1694–1710.
- Lei, Q. & Gao, K., 2018. Correlation between fracture network properties and stress variability in geological media, *Geophys. Res. Lett.*, **45**, 3994–4006.
- Martin, C.D. & Lanyon, G.W., 2003. Measurement of in-situ stress in weak rocks at Mont Terri Rock Laboratory, Switzerland, *Int. J. Rock Mech. Min. Sci.*, **40**(7–8), 1077–1088.
- Mogi, K., 2007. *Experimental Rock Mechanics*. Taylor & Francis.
- Murdoch, L.C., 1995. Forms of hydraulic fractures created during a field-test in overconsolidated glacial drift, *Quart. J. Eng. Geol.*, **28**, 23–35.
- Orellana, L.F., Scuderi, M.M., Collettini, C. & Violay, M., 2018. Frictional properties of Opalinus clay: implications for nuclear waste storage, *J. geophys. Res.*, **123**, 157–175.
- Rice, J.R., 1992. Fault stress states, pore pressure distributions, and the weakness of the San Andreas fault, in *Fault Mechanics and Transport Properties in Rocks*, pp. 475–503, eds Evans, B. & Wong, T.-F., Academic Press.
- Rutqvist, J., Chin-Fu, T. & Stephansson, O., 2000. Uncertainty in the maximum principal stress estimated from hydraulic fracturing measurements due to the presence of the induced fracture, *Int. J. Rock Mech. Min. Sci. Geomech. Abstr.*, **37**, 107–120.
- Singh, A., Rao, K.S. & Ayothiraman, R., 2019. An analytical solution to wellbore stability using Mogi-Coulomb failure criterion, *J. Rock Mech. Geotech. Eng.*, **11**(6), 1211–1230.
- Thoeny, R., 2014. Geomechanical analysis of excavation-induced rock mass behavior of faulted opalinus clay at the Mont Terri underground rock laboratory (Switzerland), *PhD thesis*, Engineering Geology Geological Institute ETH Zurich Sonneggstrasse 5 CH-8092 Zurich Switzerland, www.engineeringgeology.ethz.ch.
- Viesca, R.C. & Rice, J.R., 2012. Nucleation of slip-weakening rupture instability in landslides by localized increase of pore pressure, *J. geophys. Res.*, **117**, B03104, doi:10.1029/2011JB008866.
- Warpinski, N.R. & Teufel, L.W., 1991. In situ stress measurements at Rainier Mesa, Nevada test site—influence of topography and lithology on the stress state in tuff, *Int. J. Rock Mech. Min. Sci.*, **28**, 143–161.
- Warren, W.E. & Smith, C.W., 1985. In situ stress estimates from hydraulic fracturing and direct observation of crack orientation, *J. geophys. Res.*, **90**, 6829–6839.
- Zoback, M.D. *et al.*, 2003. Determination of stress orientation and magnitude in deep wells, *Int. J. Rock Mech. Min. Sci.*, **40**(2003), 1049–1076